Pilot-Scale Investigation and CFD Modeling of Particle Deposition in Low-Dust Monolithic SCR DeNOx Catalysts

Michael Lykke Heiredal and Anker Degn Jensen
Dept. of Chemical and Biochemical Engineering, Technical University of Denmark, Building 229, DK-2800 Kgs. Lyngby, Denmark

Joakim Reimer Thøgersen
Haldor Topsøe A/S, Nymøllevej 35, DK-2800 Kgs. Lyngby, Denmark

Flemming Jappe Frandsen
Dept. of Chemical and Biochemical Engineering, Technical University of Denmark, Building 229, DK-2800 Kgs. Lyngby, Denmark

Jens-Uwe Friemann
ANSYS Sweden AB, Vestagatan 2B, 416 64 Göteborg, Sweden

DOI 10.1002/aic.13990
Published online January 31, 2013 in Wiley Online Library (wileyonlinelibrary.com)

Deposition of particles in selective catalytic reduction DeNO$_x$ monolithic catalysts was studied by low-dust pilot-scale experiments. The experiments showed a total deposition efficiency of about 30%, and the deposition pattern was similar to that observed in full-scale low-dust applications. On extended exposure to the dust-laden flue gas, complete blocking of channels was observed, showing that also in low-dust applications soot blowing is necessary to keep the catalyst clean. A particle deposition model was developed in computational fluid dynamics, and simulations were carried out assuming either laminar or turbulent flow. Assuming laminar flow, the accumulated mass was underpredicted with a factor of about 17, whereas assuming turbulent flow overpredicted the experimental result with a factor of about 2. The simulations showed that turbulent diffusion in the monolith channels and inertial impaction and gravitational settling on the top of the monolith were the dominating mechanisms for particle deposition on the catalyst. © 2013 American Institute of Chemical Engineers *AIChE J*, 59: 1919–1933, 2013
Keywords: aerosols, catalysis, computational fluid dynamics, particle technology, deposition mechanisms

Introduction

The energy need of today's industrialized world has created major environmental problems such as emission of sulfur and nitrogen oxides, as well as submicrometer and micrometer-sized particles. A major contributor to the emission of nitrogen oxides is combustion of coal in stationary power stations.[1,2] The oxides of nitrogen are atmospheric pollutants because they contribute to formation of acidic rain, photochemical smog, destruction of the ozone layer, the greenhouse effect, and are toxic for humans. Today, significant reduction in the emissions of nitrogen oxides from combustion of pulverized coal has been achieved by primary means such as low-NO_x burners and air staging and by secondary means, that is, by post combustion flue gas cleaning of which the selective catalytic reduction (SCR) of NO_x is the most efficient and widely used.[1,3–5] In this process, ammonia or urea is injected in the flue gas allowing for reactions between NO_x and NH_3 into harmless water and nitrogen over a catalyst.

Loss of catalytic activity (deactivation) is a major problem related to operating heterogeneous catalysts. Deactivation of catalysts can occur due to a number of different mechanisms such as[3,6,7] chemical poisoning, plugging, and fouling/blinding, sintering, and loss of active components, for example, by evaporation, erosion, or attrition.

A major issue when using SCR DeNO$_x$ for both high-dust and low-dust applications of coal-fired power stations is the risk of physical deactivation due to particle (fly ash) deposition and plugging of the monolithic catalysts as well as erosion which results in a shortened catalyst lifetime. For a SCR catalyst, the high-dust position between the economizer and air preheater is the most commonly used configuration where the fly ash particle concentration in the flue gas according to Raask[8] is about 20 g/Nm^3. In low-dust applications, the SCR reactor is placed after the electrostatic filter and before the air preheater. However, even though the fly ash particle concentration is much lower ($\sim$20 mg/Nm^3) in low-dust applications compared to high-dust applications, severe plugging is occasionally observed in low-dust applications, as shown in Figure 1 for a full-scale plant. The extent

Correspondence concerning this article should be addressed to A. D. Jensen at aj@kt.dtu.dk.

Figure 1. Example of particle deposition in the SCR reactor in the low dust position of a waste incineration plant after 15,000–20,000 h of operation.

Hydraulic diameter about 3.4 mm. Courtesy Topsøe.

of deposition and plugging depends on the properties of the fly ash, the shape, and dimension of the catalyst channels, gas velocity, and flow angle among others. As deposition and plugging causes major operational problems, it is important to have a tool that can be used to understand and minimize these problems. Aerosol particle transport mechanisms depend on the characteristics of the particles (size, shape, density, and charge) and different mechanisms will dominate transport of submicrometer particles compared to larger particles. Understanding of particle transport mechanisms and deposition is, thus, important for the design of gas cleaning equipment, such as, for example, SCR $DeNO_x$ monolithic catalysts. The different transport mechanisms that are potentially active in a monolithic catalyst are the following:

- Brownian diffusion
- Turbulent diffusion
- Turbophoresis
- Inertial transport
- Thermophoresis
- Shear-induced lift
- Electrostatic forces
- Drag forces
- Gravitational forces

Young and Lemming[9] showed that particle deposition in turbulent flow is normally divided into three regimes—a diffusional deposition regime, a diffusion-impaction regime, and an inertia-moderated regime. The division into these three regimes has also been confirmed by others.[10–12] In the diffusional deposition regime, particle transport to the walls in turbulent flows is well-represented by a gradient diffusion model consisting of turbulent diffusion in the core of the tube and Brownian diffusion in a very thin region directly adjacent to the wall. In the diffusion-impaction regime, the deposition is a result of interaction between particles having significant inertia and the fluid turbulent eddies. In the inertia-moderated regime, diffusion is assumed to have little or no influence on the deposition because the very large particles acquire sufficient momentum from large eddies in the turbulent core to reach the wall. This mechanism is called turbophoresis.[10–12] Young and Lemming[9] also concluded that turbophoresis dominated the particle behavior in the diffusion-impaction and inertia-moderated regimes.

In the present study, low-dust pilot-scale experiments were conducted to investigate deposition and plugging in SCR $DeNO_x$ monolithic catalysts using commercial corrugated-type SCR monolithic catalysts obtained from Haldor Topsøe A/S. Furthermore, a particle deposition model, based on the commercial Computational Fluid Dynamics (CFD) code ANSYS-Fluent®, was developed to provide a first step toward a design tool.

Methods

Experimental methods

Commercial corrugated-type SCR monolithic catalysts with a hydraulic diameter of about 3.4 mm from Haldor Topsøe A/S were used in the experiments. The dimensions of the monolithic catalysts were 7.5 × 7.5 × 50 cm—see Figure 2. The catalysts were exposed to a dust of potassium chloride, KCl, with a diameter in the size range of 0.04–10 μm as measured by Zheng et al.,[13] and a concentration of about 19 mg/Nm^3, corresponding to low-dust conditions at

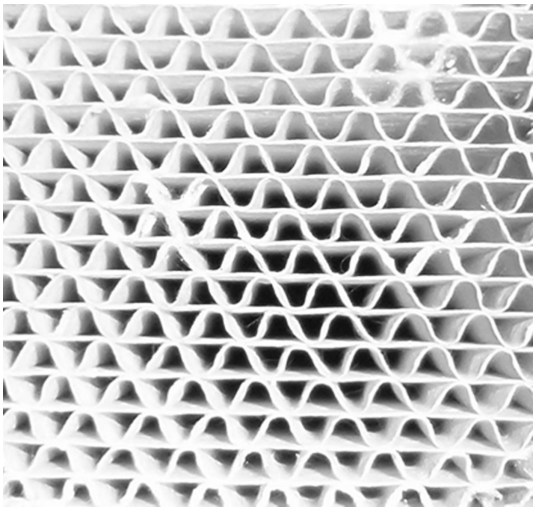

Figure 2. Topsøe DNX x30 monolithic catalyst with a hydraulic diameter of 3.4 mm that are used in the experimental investigation.

a constant temperature of 350°C. The catalysts were exposed to the dust containing gas (KCl particles) over time up to 158 h. KCl was chosen as the dust for several reasons. First of all, it is relatively easy to generate dust in the relevant particle size from a solution of KCl in water. Second, KCl is relevant for biomass applications when the SCR reactor is placed tail-end. Finally, we expect the type of material to be of less importance for the deposition compared to particle-size distribution. For each of the experiments with different exposure time, a new catalyst element was used.

Most of the experiments with exposure to KCl particles were carried out using an existing heat exchanger in the pilot plant. The experiment with 78 h of exposure to KCl particles was the last experiment carried out in the present study, and before this experiment, the pilot plant was cleaned and a new heat exchanger was installed due to corrosion of the old one. For this experiment, a much faster deposition rate was observed. It is expected that the reason for this is that fewer KCl particles were deposited in the new heat exchanger and pipes reducing the particle loss upstream of the monolithic catalyst. This created a higher particle load upstream the monolith during the 78 h experiment compared to the previous experiments. Unfortunately, the particle concentration at the inlet of the monolith for this experiment was not measured and it is, therefore, only discussed qualitatively.

Figure 3 shows a schematic illustration of the SCR pilot plant used for the deposition experiments. The pilot plant consisted of a 50 kW natural gas burner, a water-cooled lance with a two fluid (pressurized air and the liquid solution) nozzle at the outlet for injecting liquid solutions, a square duct (SCR reactor) hosting the monolithic catalyst, a soot blowing system, two different heat exchangers to adjust the temperature of the gas, and two 100 L containers for the liquid salt solution [(7.4 g/L KCl) in distilled water].

The principle of the setup was as follows: the setup ran slightly below atmospheric pressure (0–20 mbar) for safety reasons and natural gas was burned to generate a hot flue gas. The flue gas exiting the burner at about 1000–1100°C was then led to a high-temperature tube where the KCl solution was injected and an aerosol of the KCl salt was generated. The flow of the salt solution was 400 mL/h giving an injected mass flow of KCl = 8.22×10^{-7} kg/s. A bayonet heat exchanger was inserted into the main duct (high-temperature tube) downstream of the formation of the desired aerosol particles to cool down the flue gas before the unlined steel tube to avoid accelerated corrosion caused by the potassium compounds. The temperature of the flue gas at the inlet of the SCR reactor was kept at about 350°C, and the reactor was isothermal due to efficient insulation. This is also the case for an industrial reactor in operation, additionally because the heat of reaction released is very low due to the low reactant concentrations. Three soot blowers were placed just above the monolithic catalyst to blow away any fragments of old deposit from the tubing upstream of the monolithic catalyst during start up. This was done to reduce deposition on the top of the monolithic catalyst induced by these fragments and to ensure a clean monolith at the beginning of the experiments. The total flow rate at the outlet of the burner was about 60 Nm^3/h, and the flow rate through the catalyst was kept at 40 Nm^3/h, by adjusting a bypass valve. This corresponded to a channel velocity of 4.5 m/s at 350°C upstream of the catalyst. The Reynolds number based on the hydraulic diameter in the DNX x30 monolithic catalysts in the pilot-scale experiments was about 400, and the Reynolds number in the pilot-plant channel upstream the catalyst was about 6000 and, therefore, fully turbulent. Calculations based on Langhaar[14] indicate that the transition length from turbulent to laminar flow in the channels of the monolithic catalyst is about half the channel length (≈25 cm) and the flow is, therefore, expected to change from turbulent flow above the monolith to laminar flow within the channels. Turbulent eddies up to the size of the diameter of the monolithic channels would, therefore, be convected into the channels and dominate deposition in the entrance length (about half of the axial length) of the monolith. This is discussed further later.

After each experiment, the catalyst element was removed, and the deposited mass of KCl aerosol particles in the monolithic catalysts was determined by washing the monolith in ultrapure water. To determine the axial deposition profile, the monoliths were also cut in six pieces (0–1, 1–10, 10–20, 20–30, 30–40, and 40–50 cm). Each piece was washed in 5 L of ultrapure water, and 50 mL samples were sent to analysis for measuring the amount of potassium, K, in the samples. The total mass of KCl aerosol particles deposited in the monolithic catalysts was then estimated based on the equimolar ratio of K and Cl in KCl.

The total aerosol particle number concentration was measured by a Condensation Particle Counter Model 3775 TSI Incorporated each second over a period of 15 min. The

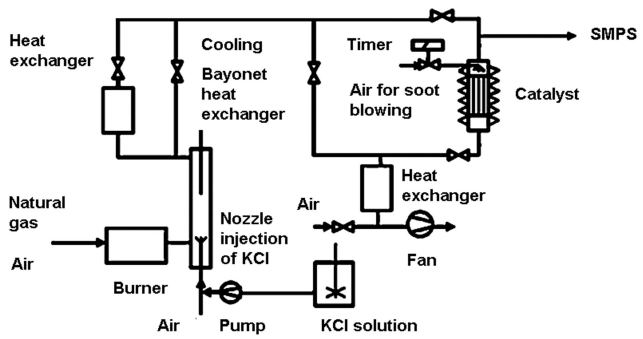

Figure 3. Schematic illustration of pilot-scale setup for monolithic catalyst deposition test.

influence of electrostatic forces in the pilot plant was investigated by measuring the average number of elementary charges, i, on the KCl aerosol particles in the pilot plant using an electrometer. The average number of elementary charges per particle, i, was measured by averaging the current measured each second by an Electrometer Model 3068B TSI Incorporated over a period of 10 min. The average number of elementary charges, i, was, $i = 0.001$, and the KCl aerosol particles were, thus, carrying a low positive average charge.

The injected mass flow of KCl particles that reaches the monolithic catalyst is considerably lower than the amount injected into the flue gas due to deposition in the duct before the catalyst element. The fraction of particles that reached the monolith was about 26% giving a mass flow just above the catalyst of about 2.1×10^{-7} kg/s. The size distribution of the particles was obtained from a previous study under the same experimental conditions.[13] The overall mass-based deposition efficiency of the particles is

$$\eta_{\text{overall}} = \frac{\dot{m}_{\text{deposit,catalyst}}}{\dot{m}_{\text{in,catalyst}}} \tag{1}$$

where $\dot{m}_{\text{deposit,catalyst}}$ is the mass flow of particles deposit in the catalyst and $\dot{m}_{\text{in,catalyst}}$ is the mass flow of particles entering the catalyst.

Numerical methods

Particle deposition assuming either laminar or turbulent flow, respectively, in the monolithic catalysts has been numerically investigated using the commercial CFD solver ANSYS-Fluent® version 12.0.1. KCl particles in the size range between 0.04 and 10 μm, based on impactor measurements,[13] were used in the simulations. The inlet concentration of KCl particles based on the 2.1×10^{-7} kg/s corresponds to a volume fraction about 4.2×10^{-9} so the effect of particle–particle interaction was neglected. Two-way coupling was used in the simulations because of the coupling between electrostatic potential, charge density, and particle distribution.

Computational fluid dynamics

Transient laminar and turbulent CFD simulations were carried out in three-dimensional (3-D) Cartesian coordinates using an Eulerian–Lagrangian reference frame. The behavior of the dispersed secondary particle phase was modeled using a discrete particle model (DPM). In the simulations of turbulent flow, the stochastic random walk model (RWM) was used to model the turbulent diffusion of the particles. The fluid flow was modeled using the continuity equation[15] and the Reynolds-averaged Navier–Stokes (RANS) equations[15] which govern the transport of averaged flow quantities with the whole scale of turbulence being modeled.

The particle force balance written in a Lagrangian reference frame is given as follows[16]

$$m_p \frac{d\vec{u}_p}{dt} = \vec{F}_{\text{drag}} + m_p \left(1 - \frac{\rho_f}{\rho_p}\right)\vec{g} + \vec{F_L} + \vec{F_B} + \vec{F_E} \tag{2}$$

where $\vec{u}_p$ is the particle velocity at position $\vec{x}$, t is the time, ρ is the fluid density, ρ_p is the particle density, and $\vec{g}$ is the gravitational acceleration vector. The first term on the right-hand side of Eq. 2 is the drag force $\vec{F}_{\text{drag}}$, the second term on the right-hand side is the Buoyancy force, the third term on the right-hand side is the shear induced (Saffman) lift force $\vec{F}_L$, the fourth term on the right-hand side is the force due to Brownian motion (Brownian force) $\vec{F}_B$, and the fifth term on the right-hand side is the electrostatic forces $\vec{F}_E$. Thermophosesis is not included as a deposition mechanism because the system is isothermal.

The 3-D version of the Saffman lift force[17,18] which is valid for small particle Reynolds numbers is given as follows[19]

$$\vec{F_L} = m_p \frac{2Kv^{1/2}\rho_f d_{ij}}{\rho_p D_p (d_{lk} d_{kl})^{1/4}} (\vec{u} - \vec{u}_p) \tag{3}$$

where d_{ij} is the deformation tensor and is defined as

$$d_{ij} = \frac{1}{2}\left(\frac{\partial u_i}{\partial x_k} + \frac{\partial u_k}{\partial x_i}\right) \tag{4}$$

Brownian motion effects are significant for submicrometer particles. The components of the Brownian force, F_{Bi}, is modeled as a Gaussian white noise process with spectral intensity, $S_{n,ij}$, given as[19]

$$S_{n,ij} = S_0 \delta_{ij} \tag{5}$$

In Eq. 5, δ_{ij} is Kronecker's delta function and S_0 is given as follows[16]

$$S_0 = \frac{216 v k_B T}{\pi^2 \rho_f D_p^5 \left(\frac{\rho_p}{\rho_f}\right)^2 C_c} \tag{6}$$

where v is the kinematic viscosity of the fluid, k_B is the Boltzmann constant, and T is the absolute temperature of the fluid. The amplitudes of the Brownian force components are given as[16]

$$F_{Bi} = \zeta_i \sqrt{\frac{\pi S_{n,ij}}{\Delta t}} \tag{7}$$

where ζ_i in Eq. 7 are zero-mean, unit-variance-independent Gaussian random numbers (three independent numbers are numerically generated for each time step) and Δt is an integration time step during the particle tracking.[19]

The drag force $\vec{F}_{\text{drag}}$, is calculated as[16]

$$\vec{F}_{\text{drag}} = m_p \frac{18\mu}{\rho_p D_p^2 C_c} \frac{C_D Re_p}{24} (\vec{u} - \vec{u}_p) \tag{8}$$

where $\vec{u}$ is the fluid velocity vector. The drag coefficient, C_D, for a spherical particle can be calculated as a function of the particle Reynolds number, Re_p from the following correlation[20]

$$C_D = \frac{24}{Re_p}(1 + 0.1806 Re_p^{0.6459}) + 0.4251 \Big/ \left(1 + \frac{6880.95}{Re_p}\right) \tag{9}$$

Turbulent flow

The whole scale of turbulence is represented through the Reynolds stresses in the RANS equations. The Reynolds stresses is modeled using the Boussinesq hypothesis to relate the Reynolds stresses to the mean velocity gradients.[16] In the present work, the k-ε model was chosen for its simplicity and robustness, computational economy and reasonable accuracy, and because it is the most validated turbulence model which gives good performance for many industrially relevant problems.[16,21]

In the turbulent cases using the DPM, the discrete stochastic RWM (or "eddy lifetime") in ANSYS-Fluent® version 12.0.1was used to simulate the dispersion of the particles. The discrete stochastic RWM includes the effect of the instantaneous turbulent velocity fluctuations on the particle trajectories through the use of stochastic methods.[16] For the Lagrangian tracking, one million particles with 10 numbers of tries and a time scale constant of 0.15 representing the mass flow of the particles were used.

Electrostatic forces

Electrostatic forces giving rise to electrostatic dispersion occurs because of the image force (polarization) between charged particles and a conductive wall (zero or constant potential), or because of electrostatic repulsion between particles charged with the same polarity (space-charge) or due to a total positive or negative average charge on a concentration of a cloud of charged aerosol particles. The space charge creates a migration of the charged particles to the boundaries of the system.

The electrostatic forces due to an electrostatic field neglecting the dielectrophoretic and the dipole-dipole force has been implemented based on Li and Ahmadi[19] as follows

$$\vec{F}_E = q\vec{E} - \frac{q^2}{16\pi\varepsilon_0 y^2}\vec{n}p \tag{10}$$

where q is the particle charge, y the distance to the wall $\vec{E}$ is the electric field strength, and $\vec{n}_p$ is the unit vector from the location of the particle to the point of the wall where the distance is shortest. The first term on the right-hand side is the Coulomb force due to an electric field and the second term on the right-hand side is the image force. Equation 10 has been implemented through the force balance on a particle given in Eq. 2. The space charge of aerosol particles each carrying a charge, q, creates a nonzero potential within the system. If the particle number concentration, n, of the aerosol particles is large, its space charge forms a continuum where the electrostatic potential, Φ, is a smooth function given by Poisson's equation as follows

$$\vec{\nabla}^2\Phi = -\frac{qn}{\varepsilon_0} = -\frac{ien}{\varepsilon_0} \tag{11}$$

where $q = ie$ is the total average charge carried by a particle, ε_0 is the permittivity of the gas phase, and n is the particle number concentration. The potential is calculated using a user-defined scalar (UDS) transport equation[16] consisting of only the diffusion term and a source term.

Simple model for particle-wall interaction

A simple quasistationary collision model based on the conservation of energy for whether a charged particle will adhere or not to the wall surface of, for example, a tube that has been grounded, is presented in the following section. The model is based on the work of Heinl and Bohnet.[22]

When a charged particle approaches a tube wall, there will be two cases, that is, the charged particle will either adhere to the wall or it will bounce. A quasistationary model is of course a rough assumption to a real collision (or dynamic collision) which would be very complicated to model because it involves dynamic energy dissipation mechanisms including radiation of photons, surface acoustic waves, stress, and flexural waves with associated viscoelastic and viscoplastic energy dissipation.[23]

Conservation of energy for a quasistationary particle-wall collision can be stated as follows

$$\text{Energy before collision} = \text{Energy after collision} + \text{loss} \tag{12}$$

Heiredal[24] gives a detailed derivation of the model. Based on the model given in Eq. 12, the critical velocity below which the particle will adhere, $w_{\text{p,crit}}$, can be calculated as follows

$$W_{\text{p,crit}} = \sqrt{\left(\frac{h\bar{\omega}}{kD_p 4\pi^2 z_0^2}\right)^2 \frac{3}{4H\rho_p} + \frac{3}{2\pi^2 D_p^3 k^2}\frac{1}{\varepsilon_0\rho_P}\left(\frac{2q_2^2}{2z_0 + D_p} - \frac{q_1^2}{l}\right)} \tag{13}$$

Equation 13 differs from Eq. 17 in the article by Heinl and Bohnet[22] by a factor of two in the denominator in the second term under the square root. The reason for this is probably that Heinl and Bohnet[22] calculate the potential energy of the particle before and after the collision with the wall by assuming a point charge at the wall and then calculate the work due to Coulombs force between these two charges. In Eq. 13, the electrostatic potential energy (the second term on the right-hand side) is calculated based on a mirror force between a charged particle and a conducting surface (grounded) and the mirror force corresponds to twice the distance to the wall from the particle, under the assumption that the wall has been grounded.[22] Equation 13 can now give the condition for adhesion of the particle if the particle velocity is smaller than the critical particle velocity as follows

$$|\vec{w}_{p,1}| \leq w_{\text{p,crit}} \tag{14}$$

Particles that reflect the wall are given a new normal and tangential velocity based on a perfect reflection from the wall.

The quasistationary collision model for particle–wall interaction was implemented in ANSYS-Fluent® version 12.0.1 based on the critical velocity, $w_{\text{p,crit}}$, given in Eq. 13 and the criteria for particle adhesion given in Eq. 14.

Numerical model

All simulations were carried out using second-order upwind discretization schemes. The simulations were initially carried out at steady state to a converged solution. Then, a time step was used to accumulate the particle mass flow on the walls. This time step was 1 h and used for the tracking (therefore, the solution was shifted to transient) but it would not influence the continuous phase, only the particle tracking to accumulate the mass of the deposit on the walls. For the transient simulations, first-order implicit time steps were used. The steady-state initial calculations were converged down to an error of 10^{-6} and for the transient calculations a maximum of 200 subiterations were used between each time step to converge the solution down to an error of 10^{-6}. Grid independence investigations of the flow simulations have not been carried out, but the grid sizes were selected to choose the best compromise between number of grid cells, computational time, and numerical errors based on the author's experience. The CFD model of the Topsøe DNX x30 monolithic catalyst can be seen in Figure 4. The grid consists of 517,400 hexahedral cells. Only two channels of the monolithic catalyst were modeled, and symmetry was assumed for the four sides of the inlet section. The

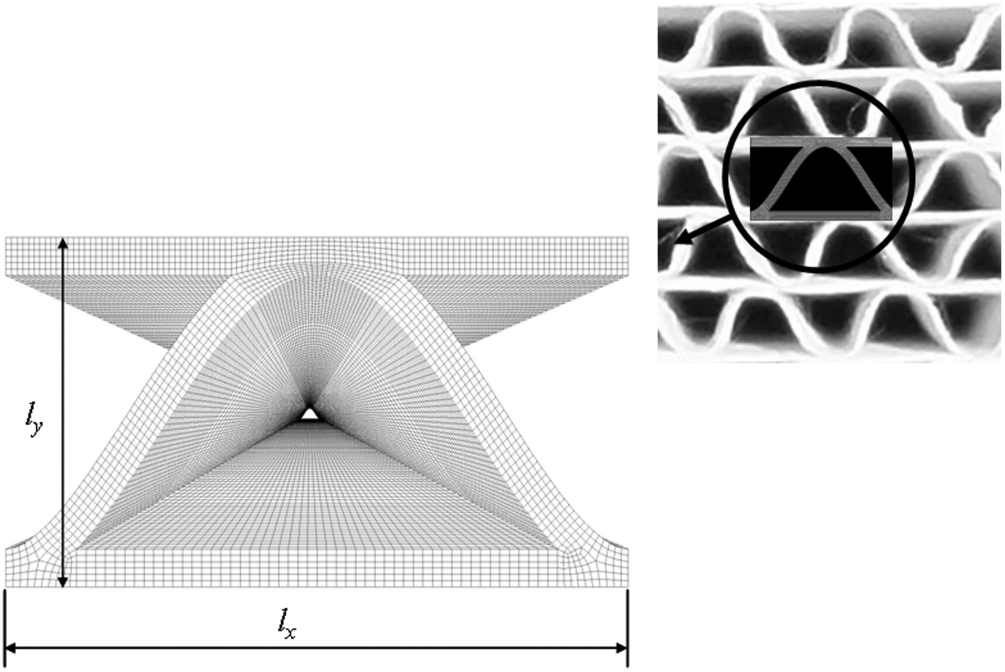

Figure 4. An illustration of the part of the catalyst of the Topsøe DNX x30 monolithic catalyst that has been modeled in the CFD calculations compared with the physical Topsøe DNX x30 monolithic catalyst geometry used in the experiments.

The total grid of the CFD model consists of 517,400 hexahedral cells and the grid is only shown on the walls of the catalyst to distinguish walls from the channel.

dimension of the model is 8.2 × 4.6 × 600 mm, and the model was extended 10-mm upstream of the channel inlet, corresponding to about 1.5-hydraulic diameter of the channel. Table 1 gives data used for the CFD simulations of the Topsøe monolithic catalyst, and Table 2 gives the model parameters for the particle–wall interaction model.

The boundary conditions of the monolithic catalyst were given as a uniform inlet velocity profile and zero gauge pressure at the outlet. A UDS transport equation transporting the electrostatic potential was given zero flux at the inlet and the walls were given zero electrostatic potential to model a grounded wall. The boundary conditions can be seen in Table 3.

The dispersed phase was given the mass flow of the individual particle diameters which were measured in the pilot plant.[13] The particle-size distribution can be seen in Table 4. In the DPM calculation, the mass flow of the individual parcels of particles was given at the injection surface, and the injected parcels of particles were stochastically distributed over the injection surface. The separation distance due to the asperities between the particle and the wall, z_0, was set to a low value of 4×10^{-15} m to reduce bouncing at the top of the catalyst as would be expected for particles of the size in the current experiments. Enhanced wall treatment was used for near-wall turbulence modeling. It combines a two-layer model with standard wall functions. The two-layer model was used if the mesh was fine enough to resolve the laminar sublayer (typical $y^+ \approx 1$), otherwise standard wall functions were used.[16]

Table 1. Data Used for the CFD Simulations of the Topsøe "sinus" DNX x30 Monolithic Catalyst

Catalyst length	0.5	[m]
Portion of the catalyst width, l_x	$8.2.10^{-3}$	[m]
Portion of the catalyst height, l_y	$4.6.10^{-3}$	[m]
Hydraulic diameter DNX x30	$3.4.10^{-3}$	[m]
Dynamic viscosity of air, μ	$3.11.10^{-5}$	[kg/(m-s)]
Kinematic viscosity of air, v	$5.51.10^{-5}$	[m^2/s]
Density of gas, ρ_f	0.56	[kg/m^3]
Pressure, p	101325	[Pa]
Temperature, T	623.15	[K]
Density of KC1 particles, ρ_p	1950	[kg/m^3]
Average velocity above channel	4.56	[m/s]
Average velocity in channel	6.5	[m/s]
Reynolds number in channel	400	[−]

Results and Discussion

Experimental results

Figure 5 shows a SEM picture of the KCl aerosol particles deposited on the outer surface of the monolithic catalyst

Table 2. Model Parameters for Particle–Wall Interaction Model

Separation distance, z_0	$4{\cdot}10^{-15}$	[m]
Strength of the wall material, H	$250{\cdot}10^{6}$	[MPa]
Liffschitz-van der Walls constant, $h\bar{\omega}$	$4{\cdot}10^{-19}$	[J]
Coefficient of restitution, K	1	[−]

Table 3. Boundary Conditions Used for the CFD Simulations of the Monolithic Catalyst

Inlet velocity	4.56	[m/s]
Inlet temperature	623	[K]
Inlet flux of electrostatic potential	0	[V/m^2-s]
Inlet hydraulic diameter (only turbulent)	$5.89.10^{-3}$	[m]
Inlet turbulence intensity (only turbulent)	10	[%]
Gauge pressure outlet	0	[Pa]
Electrostatic potential at walls	0	[V]
Reflecting walls	−	[−]

Table 4. Boundary Conditions for the Injected Particles Used for the Discrete Particle Model in the CFD Simulations of the Pilot-Scale Experiment

Particle diameter [μm]	Particle number concentration [#/m^3]	Particle mass concentration [kg/m^3]	Particle volume flow [m^3/s]	Particle mass flow [kg/s]
0.039	$2.09\cdot10^{12}$	$1.27\cdot10^{-7}$	$1.12\cdot10^{-14}$	$2.18\cdot10^{-11}$
0.070	$9.15\cdot10^{11}$	$3.14\cdot10^{-7}$	$2.77\cdot10^{-14}$	$5.40\cdot10^{-11}$
0.115	$9.72\cdot10^{11}$	$1.49\cdot10^{-6}$	$1.31\cdot10^{-13}$	$2.56\cdot10^{-10}$
0.195	$3.66\cdot10^{11}$	$2.77\cdot10^{-6}$	$2.45\cdot10^{-13}$	$4.77\cdot10^{-10}$
0.356	$3.94\cdot10^{10}$	$1.81\cdot10^{-6}$	$1.59\cdot10^{-13}$	$3.11\cdot10^{-10}$
0.697	$2.96\cdot10^{9}$	$1.02\cdot10^{-6}$	$9.02\cdot10^{-14}$	$1.76\cdot10^{-10}$
1.397	$7.91\cdot10^{7}$	$2.20\cdot10^{-7}$	$1.94\cdot10^{-14}$	$3.79\cdot10^{-11}$
2.775	$5.57\cdot10^{6}$	$1.21\cdot10^{-7}$	$1.07\cdot10^{-14}$	$2.09\cdot10^{-1}$
5.454	$5.81\cdot10^{5}$	$9.62\cdot10^{-8}$	$8.48\cdot10^{-15}$	$1.65\cdot10^{-11}$
10	$2.01\cdot10^{5}$	$2.05\cdot10^{-7}$	$1.81\cdot10^{-14}$	$3.53\cdot10^{-11}$

KCl particle concentration and mass flow based on a linear scaling of the size distribution measured by impactor measurements[9] from 0.5 to 0.1 M KCl concentration.

after 120 h of exposure to KCl particles. The SEM picture is taken at a position 30–40 cm downstream in the axial length of the DNX x30 monolith catalyst. Figure 5 shows particle sizes which are in the order of 1 μm and consist of agglomerates of primary particles and, therefore, confirm that the particles in the experiments mainly consisted of particles between 0.1 and 1 μm in agreement with the previous measurements.[13] Figure 6 shows pictures of the top of the catalyst elements for increasing exposure time. The increased mass deposition is clearly seen from the pictures for increased exposure time to KCl particles, and the deposition pattern is similar to the type of deposition observed in full-scale low-dust applications as seen on Figure 1. For the first 48 h of exposure to KCl particles, the deposit does not change the inlet geometry of the monolith channels much and there is little influence from the deposition on the flow field. At longer exposure time, the inlet to the channels becomes narrower and more streamlined and the flow stagnation area on top of the monolithic catalyst decreases as well as the sharp corners in the channels due to deposition of KCl particles. From Figure 6, it can also be observed that there are areas on the top of the catalyst where the channels are totally plugged due to deposition of small fragments (flakes). These fragments were formed when deposits on the walls of the setup upstream of the catalyst broke off. These fragments then initiate local channel plugging and accelerated deposition on top of the catalyst. Fragments can be observed on Figure 6, for example, after 24 h and 48 h of exposure time and the results of total channel plugging due to these fragments can be identified after, for example, 78, 120, and 158 h of exposure. Although the presence of these fragments was principally undesired for this investigation, they could not be totally avoided, and would also occur in full-scale installations.

Figure 7 shows the pressure loss across the DNX x30 monolithic catalyst vs. exposure time in the pilot-scale experiments. It can be observed that the repeatability in the development of the pressure loss across the DNX x30 monolithic catalysts vs. exposure time is reasonably good except for the 78 h experiment where the heat exchanger had been changed. For this experiment, the expected higher particle concentration above the monolith catalyst due to the new heat exchanger led to a higher rate of particle deposition (see also Figure 6) and, therefore, a steeper increase in pressure loss across the catalyst over time. It can also be observed from the 78 h and 158 h of exposure to KCl particles that a maximum in the pressure loss is reached at about 1050 Pa due to the available underpressure in the pilot plant. For the 78-h experiment, this maximum in pressure was reached after about 50 h of exposure time. Because of this, it was, therefore, difficult to keep the flow rate through the catalyst constant at 40 Nm^3/h for the remaining 20 h of the experiment, and the flow rate might, therefore, have been decreasing over time making it difficult to use the results of this experiment quantitatively. It can be seen from Figure 6 that the higher particle loading for the 78-h experiment led to almost total channel plugging. Under these conditions, an accelerated deposition on the top compared to inside the channels were observed because the top layer effectively acts as a particle filter.

Figure 8 shows the total accumulated mass of KCl particles vs. exposure time up to 158 h. The deposited mass of KCl particles was about 30.3 g after 158 h of exposure time. The repeatability of the experiments is indicated by the experiments for 24 and 48 h. From Figure 8, the average deposition rate of KCl particles is about 6.3×10^{-8} kg/s which corresponds to an overall mass-based deposition efficiency η_{overall}, of about 30%. Overall, the data seem to fit to a first-order polynomial although at exposure times above 48–78 h the data may indicate a decreasing deposition rate. More experimental work would be needed to confirm this.

Figure 9 shows the accumulated mass of KCl particles on the top of the catalyst (first 0–1 cm) vs. exposure time up to 120 h and the relative deposition on the top of the catalyst with respect to the total accumulated mass in the catalyst. In general, the data showed an increasing trend in the mass deposited while the fraction deposited on the top is rather constant at 6–7%. The data point at 78 h exposure time showed a significantly higher mass of deposited KCl particles due to the expected higher particle concentration after the new heat exchanger was installed. The relative deposition on the top of the catalyst was also significantly higher due to the total plugging of the channels in the catalyst. For this reason, the data point for the 78 h of exposure time on Figure 9 gives a misleading picture of the general deposition pattern under constant flow rate in the catalyst.

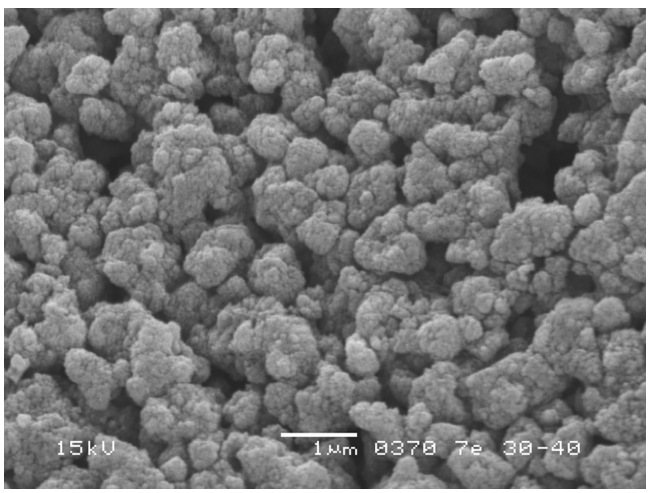

Figure 5. SEM image of KCl after 120 h of exposure.

Position 30–40 cm downstream in the axial length of the DNX x30 monolithic catalyst.

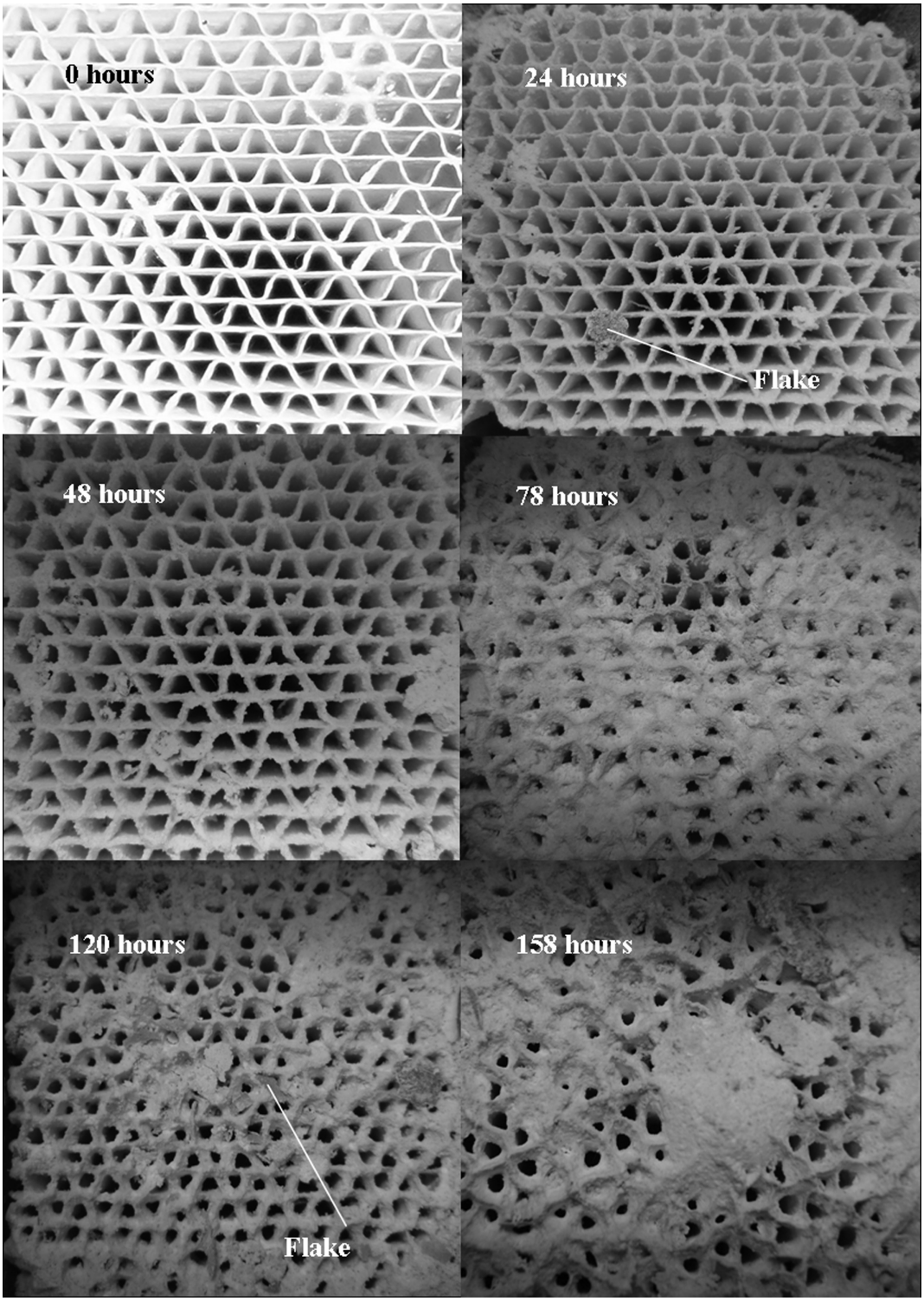

Figure 6. Plugging of SCR DNX x30 monolithic catalysts due to KCl particles after 24, 48, 120, and 158 h of exposure.

Figure 10 shows the total accumulated mass of KCl particles in the channels of the monolithic catalyst (1–50 cm) vs. exposure time up to 120 h. It can be observed that the accumulated mass deposition in the channels shows a linear build-up over time, that is, that the deposition rate is constant.

The average deposition rate in the channels of the monolith in the intervals from 1 to 10, 10 to 20, 20 to 30, 30 to 40, and 40 to 50 cm, respectively, were determined and the results are shown in Figure 11. It can be observed that for the first 48 h of exposure the average deposition rate is more or less constant along the length of the channel. Interestingly, it can also be observed that the experimental data do not seem to confirm a transition from turbulent to laminar flow in the channels of the monolithic catalyst even though this is expected at about half way down the channel length

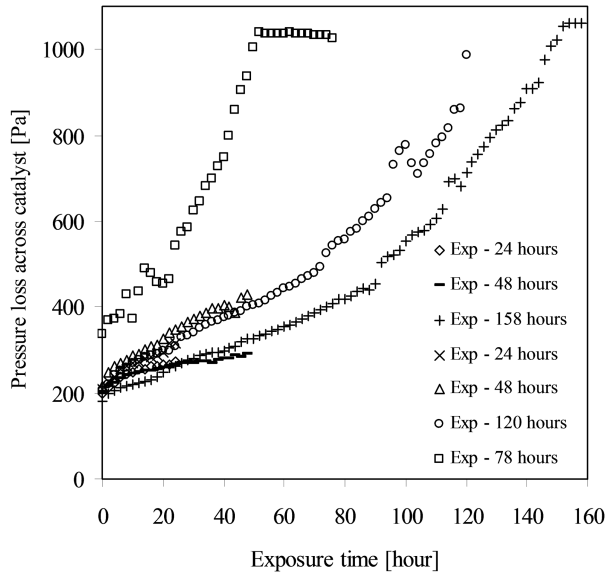

Figure 7. Pressure loss across DNX x30 monolithic catalyst vs. exposure time.

(≈25 cm). If the flow would become fully developed laminar, a considerable decrease in the average deposition rate would be expected. For longer exposure time after 78 and 120 h, there is a clear tendency of a higher deposition rate in the first part of the monolith. This supports the hypothesis that the increased average deposition rate is due to the increased Reynolds number at the inlet section, because of the reduced hydraulic diameter of the channels and the acceleration of the flow in the entrance length as well as a

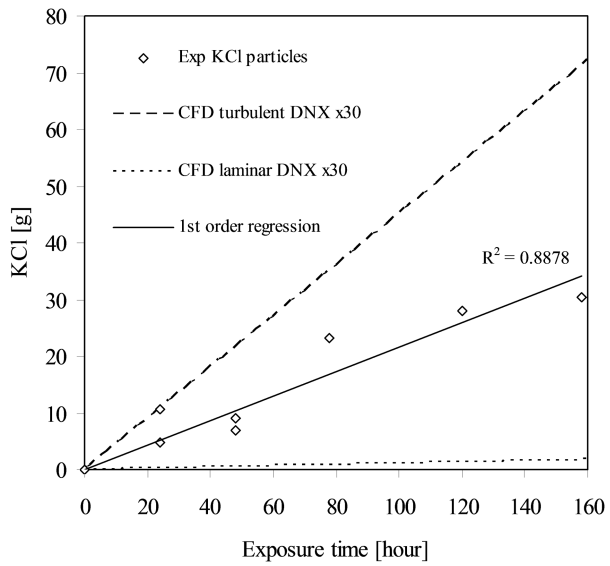

Figure 8. Experimental measurements of the total deposition of KCl particles (accumulated mass) in a DNX x30 monolithic catalyst vs. exposure time.

Volume flow, V = 40 Nm^3/h and temperature, T = 623 K. Comparison with CFD simulations of DNX x30 monolith catalyst. Average velocity above catalyst, v_{avg} = 4.56 m/s, temperature, T = 623 K, and dynamic viscosity, μ = 3.11 × 10^{-5} kg/m s. Particles modeled using DPM tracking 1.000.000 particles representing the particle-size distribution.

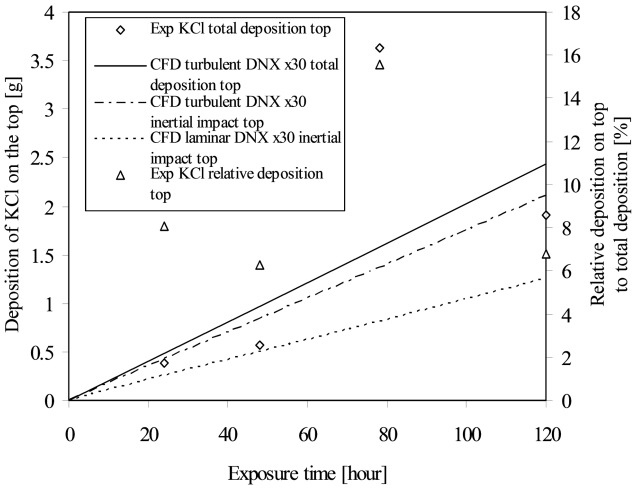

Figure 9. Experimental measurements of deposition of KCl particles (accumulated mass) on the top of a DNX x30 monolithic catalyst vs. exposure time.

Volume flow, V = 40 Nm^3/h and temperature, T = 623 K. Comparison with CFD simulations of DNX x30 monolith catalyst. Primary y axis (left) shows the total deposition on top of the catalyst. Secondary y axis (right) shows the relative deposition on top of the catalyst in relation to the total deposition. Average velocity above catalyst, v_{avg} = 4.56 m/s, temperature, T = 623 K, and dynamic viscosity, μ = 3.11 × 10^{-5} kg/m-s. Particles modeled using DPM tracking 1.000.000 particles representing the particle-size distribution.

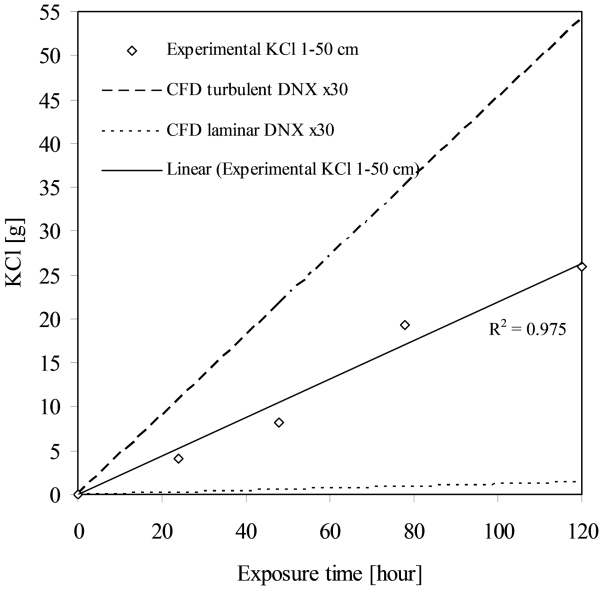

Figure 10. Experimental measurements of deposition of KCl particles (accumulated mass) on the channels of a DNX x30 monolithic catalyst vs. exposure time.

Volume flow, V = 40 Nm^3/h and temperature, T = 623 K. Comparison with CFD simulations of DNX x30 monolith catalyst. Average velocity above catalyst, v_{avg} = 4.56 m/s, temperature, T = 623 K, and dynamic viscosity, μ = 3.11 × 10^{-5} kg/m-s. Particles modeled using DPM tracking 1.000.000 particles representing the particle-size distribution.

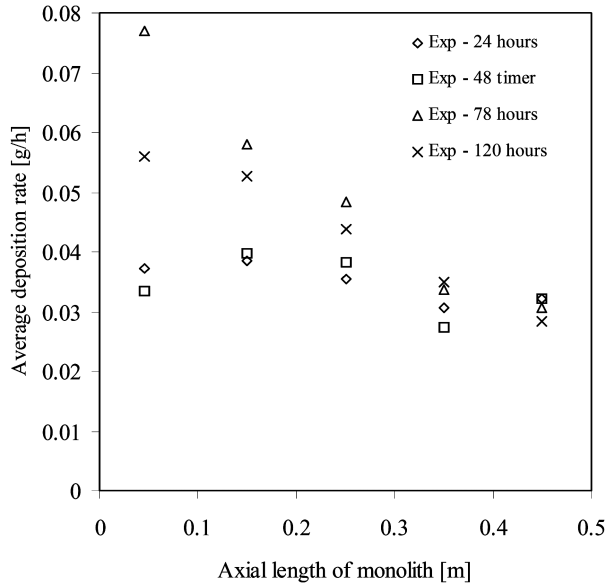

Figure 11. Average deposition rate of KCl particles in the axial length of a DNX x30 monolithic catalyst channels for 24, 48, 78, and 120 h of exposure time, respectively.

The average deposition rate has been determined in the channels of the monolith in the intervals 1–10, 10–20, 20–30, 30–40, and 40–50 cm, respectively.

larger surface area due to the deposited material. This is illustrated schematically in Figure 12 which shows the turbulent flow upstream the monolithic catalyst and turbulent eddies which are convected into the monolithic channels. Turbulent diffusion is, therefore, expected to be the dominating deposition mechanism in the monolithic channels and the influence of the increased Reynolds number is also expected to be important on the deposition mass flow in the top part of the monolithic catalyst. CFD simulations also support that turbulent flow and turbulent particle diffusion are responsible for most of the deposition observed in the pilot-scale experiments.

Comparison and discussion of experimental and CFD results

Simulations with the CFD model for prediction of particle deposition and deposit build-up in SCR $DeNO_x$ monolithic catalysts have been carried out assuming either laminar or turbulent flow fields through the monoliths to investigate the influence of the assumption of the flow type on deposition. This was done because it is computationally very demanding to model the transition from turbulent to laminar flow in the monolithic catalyst.

Table 5 shows the calculated deposition efficiency for laminar and turbulent flow in a DNX x30 monolithic catalyst element. In the laminar case, it can be observed that the deposition efficiency increases for decreasing particle diameter due to increased influence of Brownian diffusion. For increased particle diameter above about 1 mm, it can be observed that the deposition efficiency increases which is due to increased influence of the Saffman lift force which migrate the particle toward the walls. In the turbulent case, an increase in particle deposition efficiency is also observed for decreasing particle diameter due to turbulent diffusion. Increased particle deposition efficiencies are also observed for particles above about 1 mm where the larger particles gain enough momentum from the large eddies in the turbulent core and penetrate all the way to walls. As observed from Table 5, the total deposition efficiency for the DNX x30 monolithic catalyst calculated based on the CFD simulations assuming laminar flow is about 1.3% and assuming turbulent flow it is about 59.8%. For comparison, the experimentally observed deposition efficiency was around 30%. For the laminar flow case, the CFD model underpredicted the total accumulated mass with a factor of about 17 and for the turbulent flow case the total accumulated mass was overpredicted by a factor of about 2. This confirms the hypothesis that the deposition is dominated by turbulent spreading of the particles.

Figure 8 shows a comparison of the experimental results with CFD simulations of the accumulated mass of KCl particles in the catalyst. The accumulated mass of KCl particles in the CFD simulations is based on the mass deposited during each time step. As also seen in Table 5, it can be observed that the CFD simulations assuming laminar flow above the catalyst and in the channels in general underpredict the development of the accumulated mass greatly. The reason for this is that the mechanism responsible for most of the particle deposition on the top of the catalyst in laminar flow is inertial impaction and gravitational settling in the flow stagnation area (zero velocity) in front of the top of the monolithic catalyst as seen from Table 6. Inertial impaction on the top of the monolithic catalyst is responsible for about 99% of the total deposition in the monolith assuming laminar flow and corresponds to a deposition efficiency of about 1.32%. Brownian diffusion and electrostatic forces in laminar flow will only

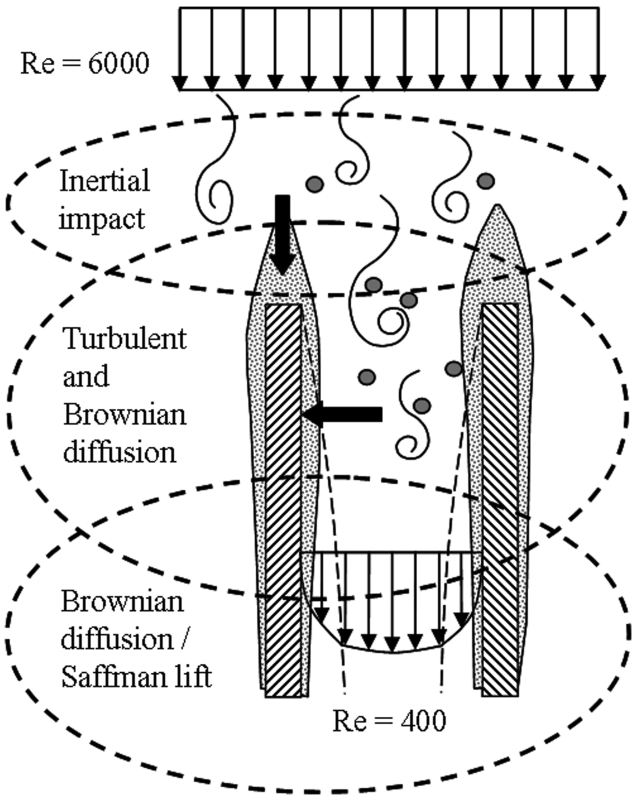

Figure 12. Schematic illustration of deposition with possible deposition mechanisms based on the pilot-scale experiments.

Ellipsis with the dashed line indicates the most important deposition mechanisms.

Table 5. CFD Simulation of the Deposition Efficiency in a DNX x30 Monolithic Catalyst for Laminar and Turbulent Flow and the Different Particle Diameters Used in the CFD Simulation

		DNX x30 Laminar flow		DNX x30 Turbulent flow	
Particle diameter [μm]	Particle Mass flow in [kg/s]	Particle mass flow out [kg/s]	Deposition efficiency [%]	Particle mass flow out [kg/s]	Deposition efficiency [%1
0.039	$2.18.10^{-11}$	$2.13{\cdot}10^{-11}$	2.5	$6.34{\cdot}10^{-12}$	70.92
0.070	$5.40.10^{-11}$	$5.37{\cdot}10^{-10}$	0.6	$1.99{\cdot}10^{-11}$	63.07
0.115	$2.56.10^{-10}$	$2.55{\cdot}10^{-10}$	0.4	$1.02{\cdot}10^{-10}$	60.02
0.195	$4.77.10^{-10}$	$4.75{\cdot}10^{-10}$	0.5	$1.98{\cdot}10^{-10}$	58.51
0.356	$3.11.10^{-10}$	$3.10{\cdot}10^{-10}$	0.5	$1.29{\cdot}10^{-10}$	58.50
0.697	$1.76.10^{-10}$	$1.75{\cdot}10^{-10}$	0.4	$8.66{\cdot}10^{-11}$	54.22
1.397	$3.79.10^{-11}$	$3.77{\cdot}10^{-11}$	0.6	$1.79{\cdot}10^{-11}$	52.67
2.775	$2.09.10^{-11}$	$2.03{\cdot}10^{-11}$	3.0	$7.07{\cdot}10^{-12}$	66.18
5.454	$1.65.10^{-11}$	$1.37{\cdot}10^{-11}$	17.1	$2.86{\cdot}10^{-12}$	82.65
10	$3.53.10^{-10}$	$2.57{\cdot}10^{-11}$	27.1	$6.99{\cdot}10^{-13}$	98.02
Total	$1.41{\cdot}10^{-9}$	$1.39{\cdot}10^{-9}$	≈1.3	$5.65{\cdot}10^{-10}$	≈59.8

spread the KCl aerosol particles slightly and due to the lack of turbulent spreading of the particles, deposition is considerably lower in laminar flow than in turbulent flow. In the channels, Brownian diffusion together with Saffman lift force and electrostatic forces will be the only mechanisms responsible for the transport of particles to the surface in laminar flow. Saffman lift force has no impact on submicrometer particles, and the electrostatic forces are weak because the average number of elementary charges only was about 0.001. Brownian particle diffusion is only important for particles less than 0.1 μm and the majority of the particles in the pilot plant are between 0.1 and 1 μm where the deposition efficiency is low as can be observed from Table 5. As it also can be seen from Table 5, inertial impaction and Saffman lift is only important for particles larger than 5 μm. The total deposition efficiency assuming laminar flow for a DNX x30 monolithic catalyst calculated based on the CFD simulations was only about 1.33% (of which about 1.32% point is on the top of the monolith and about 0.01% point is in the channels of the monolith) as seen from Table 6.

From Figure 8, it can also be observed that the CFD simulations assuming turbulent flow above the catalyst and in the channels predict the development over time in the accumulated mass better compared to the experimental results, even though the CFD simulation overpredicts the results with a factor of about 2. The reason for the overprediction is probably partly due to the fact that the CFD simulations for turbulent flow assumes turbulent flow through out the whole monolith, whereas the flow field in the physical experiments is expected to experience some loss in turbulent kinetic energy or even partly transition to laminar flow.

As seen from Figure 9, the deposition on the top of the monolith is predicted within the experimental uncertainty assuming either laminar or turbulent flow. From Figure 10, it can be observed that the total accumulated mass measured in the monolith cannot only be due to Brownian particle diffusion, inertial impaction, electrostatic forces, and Saffman lift. Because the deposition in the channel is so underpredicted in laminar flow simulations compared to turbulent flow simulations, it clearly has to be due to the contribution from turbulent diffusion in the channels of the monolith. The mass deposited on the top of the channel in the flow stagnation area upstream of the monolithic catalyst due to inertial impaction and gravitational settling is only about 2.27% in turbulent flow and is about the double compared to laminar flow (without turbulent diffusion). The reason for this is probably due to differences between the laminar and turbulent flow distribution upstream the monolithic catalyst and, therefore, small differences in the flow stagnation area on top of the catalyst. It can also be observed from Table 6 that turbulent diffusion increases the deposition efficiency for the top to about 2.7%, which is an increase in the deposition efficiency for the top with about 19% compared to inertial impaction alone.

Figure 13 shows the particle deposition flux of KCl particles assuming turbulent flow above the catalyst and in the channels of the DNX x30 monolith after one time step (1 h). Figure 14 shows a comparison of the particle deposition flux in laminar and turbulent flow, respectively. It can be observed that the particle deposition flux is significantly larger in the monolith channels assuming turbulent flow compared to laminar flow. This is due to the additional deposition mechanism from turbulent diffusion which is much larger than Brownian diffusion. It can also be observed that in the case assuming turbulent flow the particle deposition flux is very low for the first 1 or 2 cm of the channel. This can be explained from Figures 15 and 16 where Figure 15 shows the development in

Table 6. CFD Simulation of the Deposition Efficiency in a DNX x30 Monolithic Catalyst for Laminar and Turbulent Flow

DNX x30 monolith	Laminar flow Deposition efficiency [%]	Turbulent flow Deposition efficiency [%]
Top: Inertial impact	1.32	2.27
Top: Inertial impact and Brownian diffusion	1.33	–
Top: Inertial impact and turbulent Diffusion	–	2.71
Top: Inertial impact, turbulent diffusion, Saffman lift and electrostatic forces	1.33	2.71
Channel: Inertial impact, turbulent diffusion, Saffman lift and electrostatic forces	0.01	
Top and Channel: Inertial impact, turbulent diffusion, Saffman lift and electrostatic forces	1.33	59.8

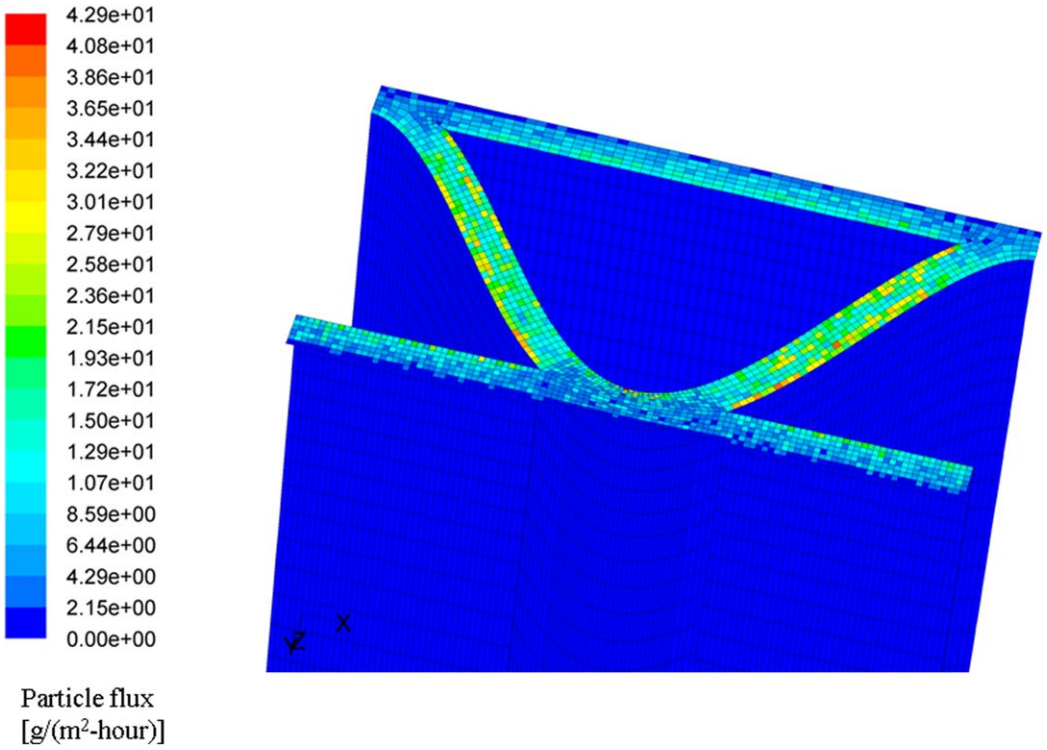

Figure 13. CFD simulation of particle deposition flux on the top of a DNX x30 monolith with turbulent flow after 1 h.

Average velocity above catalyst, v_{avg} = 4.56 m/s, temperature, T = 623 K, and dynamic viscosity, $\mu = 3.11 \times 10^{-5}$ kg/m-s. Particles modeled using DPM tracking 1.000.000 particles representing the real particle-size distribution. [Color figure can be viewed in the online issue, which is available at wileyonlinelibrary.com.]

the particle mass concentration boundary layer in the axial length of the monolith channel after 0.1, 1, 5, 10, 15, 20, 30, and 50 mm. Figure 16 shows the development in the viscous boundary layer through contour plot of the axial velocity and scaled vectors of the secondary flow in the axial length of the monolith channel after 2, 10, and 20 mm. Due to the deposition of particles on the top of the monolith, the particle concentration in the vicinity of the walls just at the inlet is very low as seen from Figure 15. At the same time, the viscous boundary layer as seen from Figure 16 and the particle concentration boundary layer as seen from Figure 15 starts to develop. However, because the viscous boundary layer is thicker than the particle concentration boundary layer due to large Schmidt numbers and the capture of particles at the top of the monolith, the particle concentration will be very low at the beginning in the viscous boundary layer. At the same time, the bulk flow is accelerated in the entrance and due to the time it takes for the particles to be transported from the bulk flow into the viscous boundary layer (mainly due to turbulent diffusion) the particles will at the same time be convected 1 to 2 cm in the axial length of the monolith channel. Therefore, as seen from Figure 14, the particle flux toward the wall has a much higher value in the downstream direction after a couple of centimeters. The increase in the particle concentration just outside the particle concentration boundary layer but still inside the viscous boundary layer can be observed from Figure 15 after a couple of centimeters.

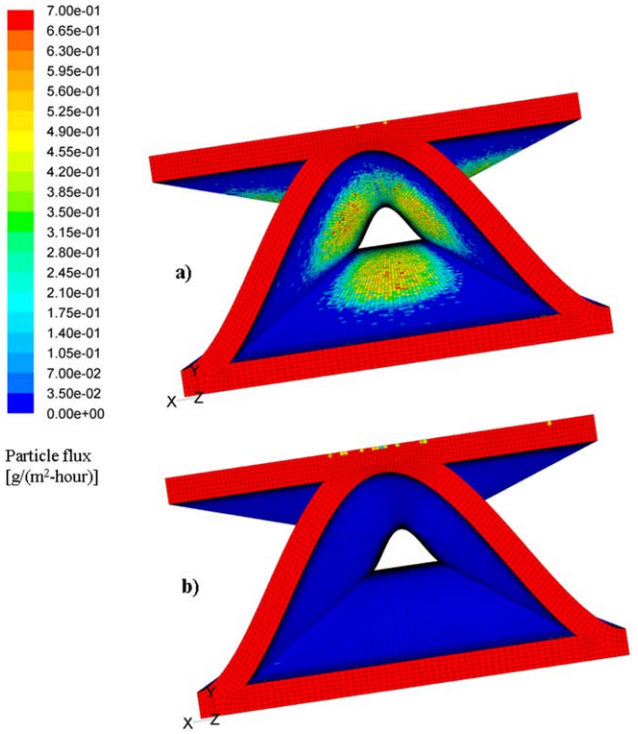

Figure 14. Contour plot of particle deposition flux in a DNX x30 monolithic catalyst after one time step (1 h) of exposure of KCl particles in (a) turbulent flow and (b) laminar flow, respectively.

[Color figure can be viewed in the online issue, which is available at wileyonlinelibrary.com.]

Conclusions

Pilot-scale KCl aerosol particle deposition experiments using commercial corrugated-type SCR monolithic catalysts

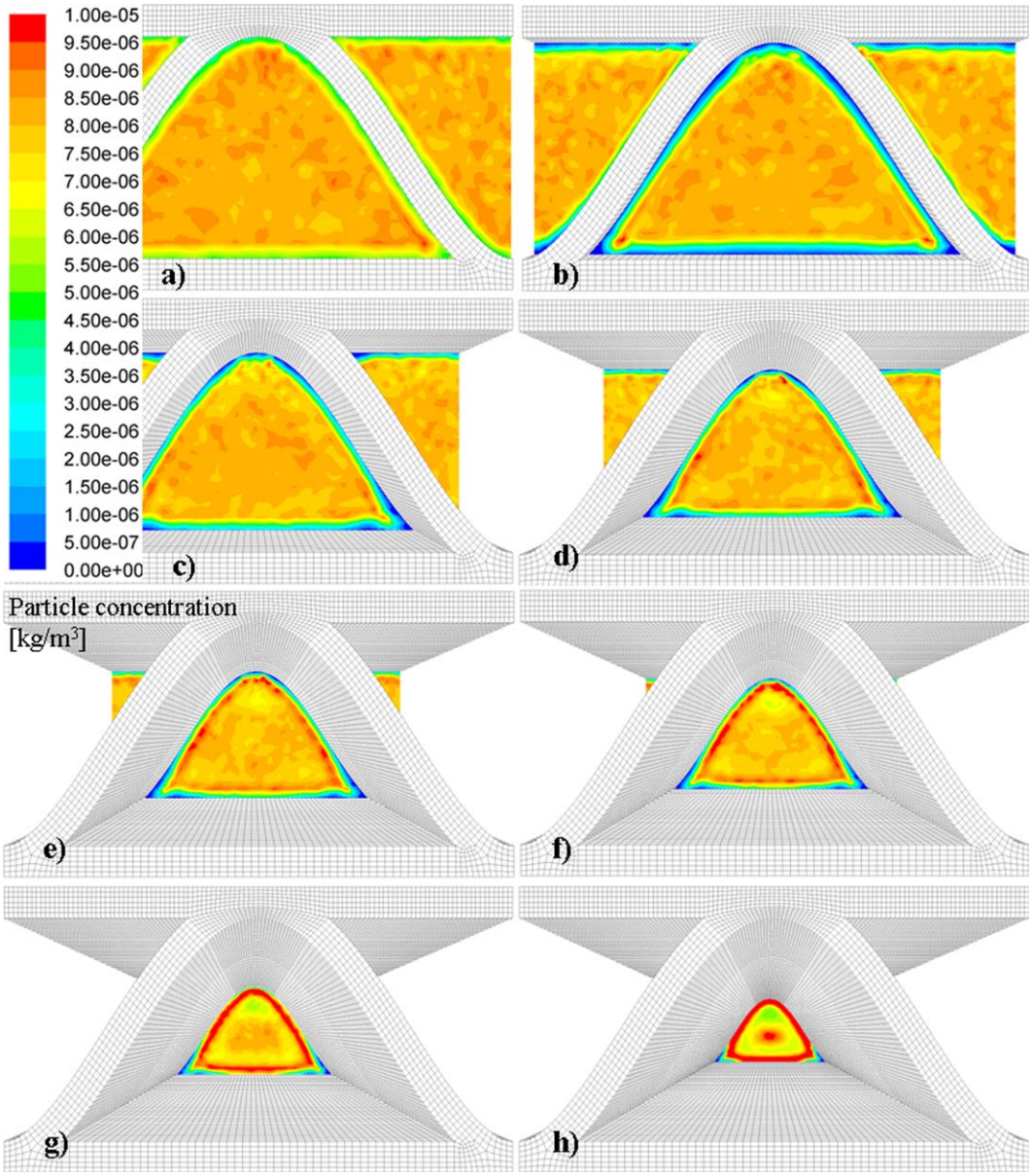

Figure 15. Particle mass concentration boundary layer in xy-planes in the axial length of the DNX x30 monolithic catalyst.

(a) After 0.1 mm, (b) after 1 mm, (c) after 5 mm, (d) after 10 mm, (e) after 15 mm, (f) after 20 mm, (g) after 30 mm, and (h) after 50 mm. [Color figure can be viewed in the online issue, which is available at wileyonlinelibrary.com.]

obtained from Haldor Topsøe A/S have been carried out under low-dust conditions. DNX x30 SCR monolithic catalysts with a hydraulic diameter of 3.4 mm were exposed to potassium chloride, KCl, particles with a size of 0.04–10 μm over time up to 158 h. The deposited mass of KCl aerosol particles in the monolithic catalysts was determined by washing out KCl of the monoliths after each experiment followed by wet chemical analysis.

The experiments showed an overall deposition efficiency of about 30%, and the deposition pattern was similar to that observed in full-scale low-dust applications. Measurements of the average deposition rate in the channels of the monolith showed that it was more or less constant along the axial length of the monolith. For longer exposure time, there was a clear tendency of a higher deposition rate in the first part of the monolith.

A particle deposition model based on the commercial CFD code ANSYS-Fluent® version 12.0.1 has been developed. Experimental data and simulation results from the CFD model, assuming either laminar or turbulent flow in the monolith, were compared and support that turbulent diffusion in the monolith channels and inertial impaction and gravitational settling in the flow stagnation area on the top of the monolith are the dominating mechanisms for deposition of particles on the catalyst surfaces and leading eventually to plugging. The simulations showed that by assuming laminar flow the deposited mass is underpredicted by a factor of about 17, whereas assuming turbulent flow overpredicted it by a factor of about 2. The CFD model may be used as a tool to predict particle deposition as a function of particle properties, operating conditions, and channel geometry and is a first step toward a design tool.

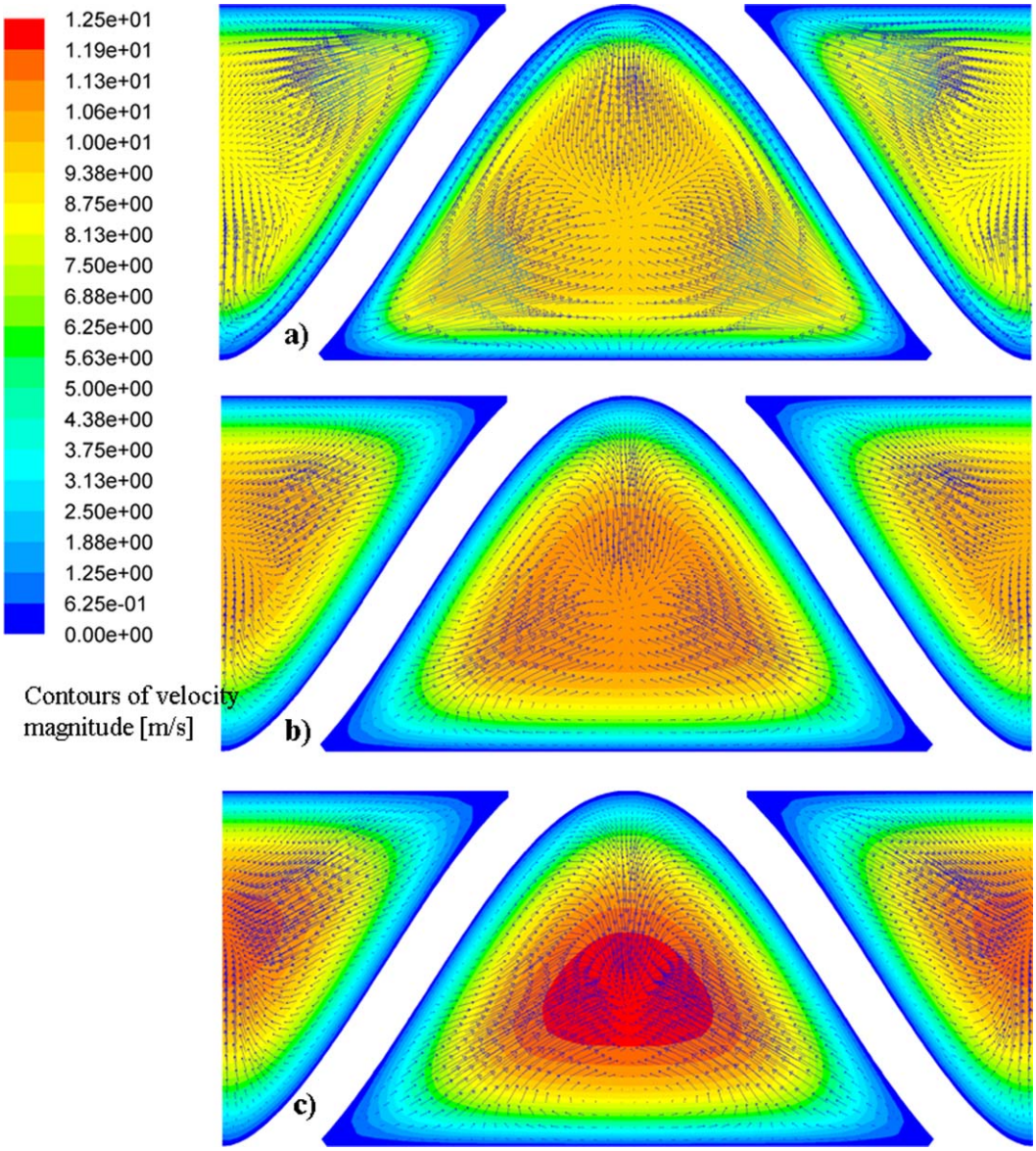

Figure 16. CFD simulation with contour plot of axial velocity and scaled vectors of the secondary flow in turbulent flow.

Illustrate the development of the viscous boundary layer. (a) Axial velocity and secondary flow after 2 mm, (b) axial velocity and secondary flow after 10 mm, (c) and axial velocity and secondary flow after 20 mm. [Color figure can be viewed in the online issue, which is available at wileyonlinelibrary.com.]

Notation

Symbols

C_c = Cunningham slip correction factor
C_D = Drag coefficient
d_{ij} = Deformation tensor, 1/s
d_{lk} = Deformation tensor, 1/s
d_{kl} = Deformation tensor, 1/s
D_p = Diameter of particle, m
e = Elementary charge, C
$\vec{E}$ = Electrostatic field strength vector, N/C
$\vec{F}_B$ = Drag force, N
F_{Bi} = Amplitudes of the Brownian force component
$\vec{F}_{\text{drag}}$ = Drag force, N
$\vec{F}_E$ = Electrostatic force, N
$\vec{F}_L$ = Saffman force, N
$\vec{g}$ = Gravitational acceleration vector, m/s^2
$h\varpi$ = Lifshitz–van der Waals constant, Nm
H = Strength of pipe wall, N/m^2
i = Number of elementary charges
k = Coefficient or restitution
k_B = Boltzmann constant, J/K
K = Saffman integration constant
l = Distance from particle to wall, m
m_p = Mass of particle, kg
$\dot{m}_{\text{deposit,catalyst}}$ = Mass flow of particles deposit in the catalyst, kg/s
$\dot{m}_{\text{in,catalyst}}$ = Mass flow of particles deposit in the catalyst, kg/s
n = Particle number concentration, #/m^3
$\vec{n}_p$ = unit vector
q = Particle charge, C
q_1 = Charge on particle before wall collision, C
q_2 = Charge on particle after wall collision, C
$S_{n,ij}$ = Spectral intensity of Brownian force, m^2/s^3
T = Fluid temperature, K
$\vec{u}$ = Fluid velocity, m/s
u_i = Fluid velocity tensor, m/s
u_k = Fluid velocity tensor, m/s
$\vec{u}$ = Fluid velocity vector, m/s
$\vec{u}_p$ = Particle velocity vector, m/s
$w_{p,1}$ = Particle velocity before particle-wall collision, m/s
$w_{p,crit}$ = Critical particle velocity for particle-wall adhesion, m/s

x_i = Cartesian tensor, m
x_k = Cartesian tensor, m
y = Distance to wall (m)
z_0 = Distance at contact, m

Greek letters

∂ = Partial differential operator
Δt = Integration time step during particle tracking, s
η_{overall} = overall mass based deposition efficiency
ρ_f = Density of fluid, kg/m^3
ρ_p = Density of particle, kg/m^3
ν = Kinematic viscosity of fluid, m^2/s
μ = Dynamic viscosity of fluid, Pa s
δ_{ij} = Kronecker's delta
ζ_i = Zero-mean unit-variance-independent Gaussian random numbers
ε_0 = Permittivity of free space, AsV^{-1} m^{-1}
Φ = Electrostatic potential, V
$\vec{\nabla}^2$ = Laplacian operator

Subscripts

B = Brownian
d = Drag
E = Electrostatic
i = General index in tensor notation
j = General index in tensor notation
k = General index in tensor notation
l = General index in tensor notation
L = Saffman lift
p = Particle

Literature Cited

1. Bosch H, Janssen F. Catalytic reduction of nitrogen oxides—a review on the fundamentals and technology. *Catal Today*.1988;2:369–532.
2. Delmas R, Serça D, Jambert C. Global inventory of NO_x sources. *Nutr Cycl Agroecosys*. 1997;48:51–60.
3. Forzatti P, Lietti L. Recent advances in De-NO_xing catalysis for stationary applications. *Heterogen Chem Rev*. 1996;3:33–51.
4. Forzatti P, Lietti L. Catalyst deactivation. *Catal Today*. 1999;52:165–181.
5. Nakajima F, Hamada I. The state-of-the-art technology of NO_x control. *Catal Today*. 1996;29:109–115.
6. Soud HN, Fukasawa K. Developments in NO_x Abatement and Control. London, UK: IEACR/89 IEA Coal Research, 1996.
7. Beeckman JW, Hegedus LL. Design of monolith catalysts for power plant NO_x emission control. *Ind Eng Chem Res*. 1991;30:969–978.
8. Raask E. Mineral Impurities in Coal Combustion: Behavior, Problems and Remedial Measures. UK: Taylor & Francis, 1985:373.
9. Young J, Leeming A. A Theory of particle deposition in turbulent pipe flow. *J Fluid Mech*. 1997;340:129–159.
10. Guha A. A unified Eulerian theory of turbulent deposition to smooth and rough surfaces. *J Aerosol Sci*. 1997;28(8):1517–1537.
11. Guha A. Transport and deposition of particles in turbulent and laminar flow. *Annu Rev Fluid Mech*. 2008;40:311–341.
12. Guha A. A generalized mass transfer law unifying various particle transport mechanisms in dilute dispersion. *Heat Mass Transf*. 2008;44(11):1289–1304.
13. Zheng Y, Jensen AD, Johnsson JE, Thøgersen JR. Deactivation of V_2O_5-WO_3-TiO_2 SCR catalyst at a biomass-fired combined plants: elucidation of mechanisms by lab- and pilot-scale experiments. *Appl Catal B*. 2008;83:186–194.
14. Langhaar HL. Steady flow in the transition length of a straight tube. *J Appl Mech*. 1942;9:A55–A58.
15. Hughes WF, Brighton JA. Fluid Dynamics, 3rd ed. New York: Schaums Outline Series, McGraw-Hill, 1999.
16. ANSYS Fluent 12.0, Theory Guide. ANSYS. Inc., 2009.
17. Saffman PG. The lift on a small sphere in a slow shear flow. *J Fluid Mech*. 1965;22(2):385–400.
18. Saffman PG. Corrigendum to "The lift on a small sphere in a slow shear flow". *J Fluid Mech*. 1968;31:624.
19. Li A, Ahmadi G. Dispersion and deposition of spherical particles from a point source in a turbulent channel flow. *Aerosol Sci Technol*. 1992;16:209–226.
20. Haider A, Levenspiel O. Drag coefficient and terminal velocity of spherical and nonspherical particles. *Powder Technology*. 1989;58:63–70.
21. Versteeg HK, Malalasekera W. An Introduction to Computational Fluid Dynamics. The Finite Volume Methods, 2nd ed. Harlow, England: Prentice Hall, 2007:80.
22. Heinl E, Bohnet M. Calculation of particle-wall adhesion in horizontal gas-solid flow using CFD. *Powder Technol*. 2005;159:95–104.
23. Dahneke B. Particle bounce or capture—search for an adequate theory: I. conservation-of-energy model for a simple collision process. *Aerosol Sci Technol*. 1995;23:25–39.
24. Heiredal ML. Particle Dynamics in Monolithic Catalysts. Ph.D. Thesis, Department of Chemical and Biochemical Engineering, Technical University of Denmark, 2010.

Manuscript received Nov. 25, 2011; and revision received Dec. 3, 2012